



# Wavelet transform based non-hermitian symmetry OFDM technique for indoor MIMO-VLC system with an imaging receiver

Arslan Khalid<sup>1</sup>

Accepted: 16 August 2021 / Published online: 26 August 2021

© The Author(s), under exclusive licence to Springer Science+Business Media, LLC, part of Springer Nature 2021

## Abstract

Recently, to increase the data capacity of visible light communication (VLC) systems naturally, an ideal combination of orthogonal frequency division multiplexing (OFDM) and multiple-input multiple-output (MIMO-OFDM) technique has proven to be an efficient way. However, to ensure real-valued output for the VLC system, a Hermitian symmetry (HS) is usually levied in the OFDM technique, which reduces the data rate while increasing the computational complexity (CC) of the system. In this paper, a wavelet transform (WT) based non-HS OFDM technique (NHS-OFDM) for the MIMO-VLC system has been presented using non-imaging and imaging receivers to study the performance numerically. The state-of-the-art NHS-OFDM technique was realized by isolating real and imaginary parts of traditional RF-based OFDM signal and then transmitted by a pair of white LED luminaries. By incorporating WT with the OFDM technique, the error performance and data rate of the system are greatly improved, as WT eliminates standard usage of the cyclic prefix. Link-level performance of the recommended MIMO-VLC system was tested, considering BER, CC, and PAPR. Also, closed-form analytical BER expressions were derived and compared with the simulated results in the presence of line-of-sight links. Analytical and simulated results are analogous to each other and confirm that the proposed WT-based NHS-OFDM technique with imaging receiver achieves better BER results, with very low CC. Moreover, the WT-based NHS-OFDM technique also reduces the PAPR without employing any reduction technique.

**Keywords** Bit-Error-Rate (BER) · Computational complexity (CC) · Non-Hermitian symmetry (NHS) · Multiple-input multiple-output (MIMO) · Peak-to-average power-ratio (PAPR) · Wavelet Transform (WT)

## 1 Introduction

Owing to a mighty surge in internet-connected, and intelligent multimedia-capable wireless devices, the telecommunication industry had merely witnessed an incredible escalation in connectivity demands. In this modern era of smart computing, people are typically practicing to associate their daily usage of physical devices with reliable internet, and this vogue will be flourishing shortly. Mostly, the data usage over physical devices is high-definition (HD) virtual and augmented (VR/AR) video streaming and

other cloud-based amenities. It is also foreseeable that by the end of 2021, specific claims for high data rate services by active users will increase dramatically; therefore, the current 4G fourth-generation mobile standard cannot sustain the breakneck pace of this upsurge [1].

To amply satisfy excessive physical device connectivity demands from active users, fifth-generation 5G, and beyond are paving their effective way to promptly becoming the potential communication technologies in upcoming mobile telecommunication standards. 5G communications offer massive device connectivity with extremely high capacity, adequate security, and excellent quality of service (QoS), trivial end-to-end delays, and seamless user mobility [2–4]. These amenities typically demand a broad radio-frequency spectrum, which in turn is exhausted and curbs the network in providing the concurrent delivery of numerous services to multiple users.

✉ Arslan Khalid  
enr.arslan08@gmail.com

<sup>1</sup> School of Information, Computer, and Communication Technology, Sirindhorn International Institute of Technology, Thammasat University, Pathum Thani 12000, Thailand

In place of radio frequency-based wireless technology, principal investigators and leading practitioners are eagerly seeking newer technologies, and Visible Light Communications (VLC) miraculously appears as a key catalyst to accelerate this successful revolution for short-range communications. Over the preceding decade, innovative VLC technology has evolved rapidly and is now very mature. A VLC transmitter exploits driver circuitry and monochromatic Light Emitting Diodes (LEDs) for both direct illumination and simultaneous conveyance of high-speed data communications [5]. While receiver typically includes photodiodes and an amplifier circuit for direct detection of an information signal. Therefore, the net cost of the system is very low when compared with radio-frequency-based systems. The additional benefits of VLC in general are: (1) unregulated, license-free spectral range, typically 10,000 times larger than radio-frequency range; (2) inherent privacy since the light signal is confined in a room; (3) intriguing possibility of successful integration with existing lighting infrastructure; (4) negligible interference with other communication technologies, and sensitive electronic components; (5) high directionality, and containment that results in excellent signal-to-noise ratio (SNR), and (6) human-friendly [5–8].

## 1.1 Related papers

In spite of the many inherent benefits of VLC technology, there are still many technical glitches that prevent the usage of VLC physically. Notable among these is the restricted modulation bandwidth of LED, which curbs the capacity of the VLC system. Up to now, many schemes have been disclosed to address this issue, including pre and post-equalization [9], spectral-efficient OFDM [10, 11], adaptive modulation [12], and multiple-input multiple-output (MIMO) [13, 14]. By combining some of these techniques, such as OFDM-based MIMO, the data rate of the VLC system can be further increased. Recently, for the VLC systems, OFDM and its variant have been adopted widely because of their high spectral efficiency and robustness against multipath fading. Unlike radio-frequency-based systems, the VLC system mainly works with intensity modulation/direct detection (IM/DD). In IM/DD, data bits modulate the luminous intensity or active power of the light beam from a light source, therefore, phase details are not mandatory.

For compatibility with LED, modulated OFDM waveform needs to be positive and real-valued, which is targeted by enacting the Hermitian symmetry (HS) into the system design before proper execution of inverse fast Fourier transform (IFFT) [15]. Conversely, it is identified that arbitrary imposition of HS can increase the standard IFFT and FFT sizes by two times, which in turn increases the

computational complexity (CC) and necessary power of the transceiver. Moreover, the possible capacity of the VLC system is also reduced. A dire necessity for an alternative technique can conveniently provide the real-valued and positive modulating waveform without strictly compromising CC and capacity of the system. In this connection, Moreolo et al., in [16], acquaints with a discrete Hartley transform (DHT) based OFDM system. Authors successfully replace the Fourier processing with real Hartley processing that circumvents HS constraint and thus provisions twofold input symbols. Nevertheless, twofold input symbols are attained only for real constellations.

Later, a novel FFT/IFFT size efficient based optical OFDM system is numerically testified in [17] and experimentally demonstrated in [18] that exploits the multiplexing of real and imaginary parts of the traditional OFDM waveform in the time domain. By doing this, size of FFT/IFFT is reduced by half, but at the same time, two consecutive symbols are required to transmit a single OFDM frame, which also limits the achievable data rate. In [19], a similar non-HS-based OFDM (NHS-OFDM) system is proposed and implemented using wavelet transforms (WT) instead of Fourier transform. By using WT, the author succeeds in improving the BER, CC, and PAPR results. However, the problem of transmitting two successive symbols within a single OFDM frame is not solved.

The fundamental idea of separately communicating the real and imaginary parts of the complex-valued OFDM signal using two RGB LED chips was wisely given by Afgani et al. [10]. Even though cited authors succeeded in eliminating the practical use of HS in transceiver design, the cost of the developed system is ultimately much higher since RGB LEDs are expensive compared to phosphor LEDs. To fully illuminate a standard room, several white LEDs are usually placed in the plastered ceiling, making the basic idea of MIMO systems realizable for the VLC systems. Standard MIMO schemes like repetition coding (RC) [20], spatial multiplexing (SMP) [21], and modified space-time block coding (STBC) [14] are repeatedly exploited to typically enhance the reliability and capacity of the VLC systems.

Observing the significant merits of aforesaid practical MIMO schemes, Chen et. al, brought into light the NHS-OFDM technique for the MIMO-VLC system [22]. The state-of-the-art NHS-OFDM technique is implemented as a result of transferring the real and imaginary parts of modulated OFDM waveform from two separate antennas. Even with NHS-OFDM, the system still uses the cyclic prefix (CP) or guard intervals to allay ISI, which undoubtedly appears as overhead, and confines from reaching the achievable data rates. Although the work gives convincing coverage results, depending on the algorithm used for IFFT/FFT, the authors obtained a reduced or

almost the same CC compared to the HS-OFDM-based MIMO-VLC system. Also, desired PAPR results, which are of utmost concern in OFDM-based systems, were not included. The poor FFT/IFFT response of filter-banks in the OFDM system causes spectral leakage [23], and 13 dB low sidelobes [24], create it extra susceptible to interference.

## 1.2 Contribution

Motivated by prior mentioned discussions, core contribution and possible outcomes of current work are tallied as,

- 1 *Proposal of Wavelet Transform-based NHS-OFDM technique for MIMO-VLC system:* Current work addresses the shortcomings mentioned in [22] and presents the WT-based NHS-OFDM technique for the MIMO-VLC system, which swaps traditional FFT/IFFT blocks in the OFDM transceiver design. By introducing wavelet functions in the VLC system, an overall capacity can be enhanced, thanks to the two-dimensional processing capability of multiresolution analysis (MRA); thus, the main issue of CP is accurately managed. Moreover, because WT is inherently orthogonal, spectrally confined sidelobes, and wavelet decomposition symbols, that overlap both in time and frequency domain helps in restraining the inter-symbol interference, inter-carrier interference, and PAPR [25].
- 2 *Development of MIMO-VLC system using NImR and ImR:* Typically, MIMO techniques are used to attain higher data rates and spectral efficiencies, yet, the MIMO-VLC systems suffer from the issue of high spatial correlation in MIMO-VLC channels [26]. To efficiently dealt with this issue, the use of imaging receivers (ImR) in MIMO-VLC system design is inevitable. ImR can easily reduce the correlation in the channel gain matrix by exploiting an imaging lens that can demultiplex the signals coming from other light sources. Hence, ImR is incorporated with the MIMO-VLC system, and the effect of utilizing NImR and ImR receivers for the MIMO-VLC system is investigated in this study. A zero-forcing scheme is implemented for both receivers, while performance comparison is accomplished considering BER curves.
- 3 *Analytical contributions:* Precision of the proposed WT-based NHS-OFDM technique for the MIMO-VLC system is confirmed by deriving analytical closed-form BER expressions over the line-of-sight link (LOS). Analytical BER expressions are derived for both NImR and ImR. To perform a valid comparison, current work additionally provides analytical closed-form BER expression for conventional FT-based NHS-OFDM

technique and then correlates it with analytical BER of the proposed technique.

- 4 *Performance indicators:* Proposed WT-based NHS-OFDM technique for the MIMO-VLC system has compared with the conventional MIMO-VLC systems by considering BER, CC, and PAPR as key performance indicators. Computerized programs for simulations of conventional and proposed techniques are formulated in the MATLAB tool.
- 5 *Key findings:* Considering LOS link configuration, the performance of conventional and proposed techniques for the MIMO-VLC system using NImR and ImR are examined by Monte-Carlo simulations. Analytical and simulated outcomes overlapped with each other illustrating the validity of theoretical calculations. Additionally, both analytical and simulated results also demonstrate that the proposed WT-based NHS-OFDM technique achieves better BER results in comparison with conventional techniques. Work also acquaints with mathematical expressions that help to determine the CC of the MIMO-VLC system. CC for the proposed WT-based NHS-OFDM technique is lower than the conventional techniques. Low PAPR results are also observed in the proposed system without exploitation of any reduction technique.

## 1.3 Paper organization

The complete paper is assembled from the following sections: Sect. 2 gives a comprehensive explanation of the proposed WT-based NHS-OFDM technique for the MIMO-VLC system. This section also highlights the indoor MIMO-VLC system model with ImR and presents the optical channel matrix. Discussions on wavelet analysis are also part of this section. Section 3 renders analytical closed-form BER expressions for the techniques that are under consideration for the MIMO-VLC system. Section 4 confers simulation setup and MATLAB-based numerical results for conventional and proposed techniques used to develop MIMO-VLC systems. Finally, Sect. 5 places out the conclusion of this paper.

## 2 NHS-OFDM based MIMO-VLC system

This section sufficiently familiarizes with the standard MIMO-VLC system developed using traditional FT and proposed WT-based NHS-OFDM techniques. For the sake of simplicity, a  $2 \times 2$  MIMO-VLC system has been conceived by engaging both NImR and ImR.

### 2.1 Modeling of MIMO-VLC system

For the MIMO-VLC system, typically, two different types of receivers imaging (ImR) and non-imaging (NImR) can be used. The graphical demonstration of the MIMO-VLC system engaging both ImR and NImR is exemplified in Fig. 1. Channel matrix obtained with NImR can be expressed by,

$$H_{NImR} = \begin{bmatrix} h_{11} & h_{12} \\ h_{21} & h_{22} \end{bmatrix} \tag{1}$$

where  $h_{pl}(l, p = 1, 2)$  denotes optical channel gain among  $l$ -th LED and  $p$ -th photodiode. Transmitting real and imaginary parts of OFDM modulated signal through different VLC transmitters will become similar to SMP, which leads to the formation of two parallel serial-input serial-output (SISO) data transmission schemes. In such transmission schemes, to eradicate ICI, transmitter-receiver pair alignment turns into a big challenge [27]. Therefore, NImR is replaced by ImR. The optical channel matrix with ImR is transformed to a diagonal matrix, which is specified as follows,

$$H_{ImR} = \begin{bmatrix} 0 & h_{12} \\ h_{21} & 0 \end{bmatrix} \tag{2}$$

A typical room environment is fitted out with multiple luminaires that are fixed on the plastered ceiling, and photodiodes are connected to portable devices, capable of detecting both directional/line-of-sight (LOS) and non-LOS (NLOS) links. The optical intensity received through the LOS link is substantially higher than the NLOS link; as a result, it is appropriate to focus entirely on the LOS link [28]. In addition, the typical wavelength of optical spectrum ranges between 380 nm to 740 nm, which is

considerably smaller when compared to the operative range of photodiode, so multipath fading is also overlooked due to very high spatial diversity. LOS channel gain by making use of generic radiation pattern for a LED can be formulated as follows [26, 28],

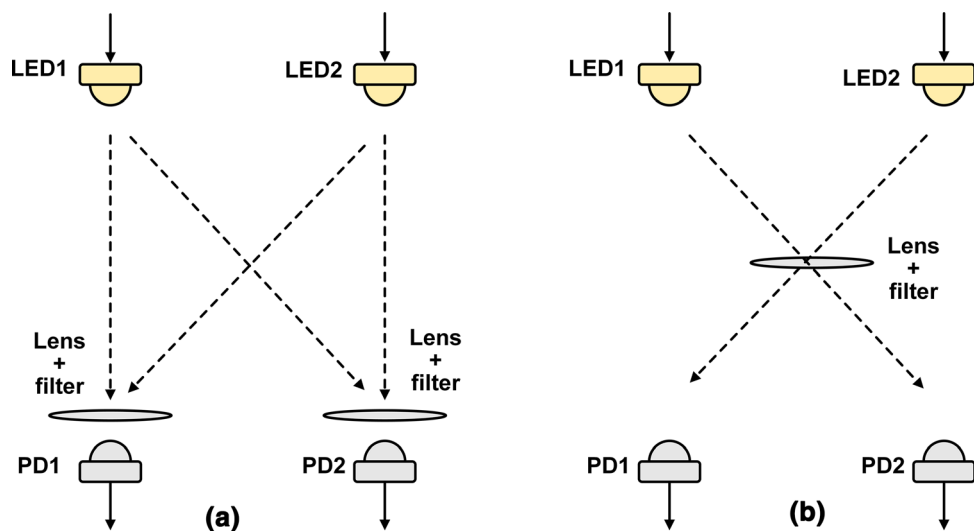
$$h_{pl} = \frac{(m_r + 1)A_{eff}}{2\pi d_{pl}^2} \cos^{m_r}(\varphi_{pl}) \cos(\phi_{pl}) \zeta \eta \tag{3}$$

where  $A_{eff}$  signifies the operative area of the lens,  $d_{pl}$  denotes LOS separation amongst centroid of  $l$ -th luminaire and centroid of the aperture of  $p$ -th lens,  $m_r = -\ln(2)/\ln(\cos(\Psi_{1/2}))$  indicates the mode number of Lambert’s radiating lobe,  $\Psi_{1/2}$  connotes LED’s half-power at semi-angle,  $\zeta$ , and  $\eta$  express the optical filter and lens gains, whereas  $(\varphi_{pl})$  and  $(\phi_{pl})$  characterizes the irradiance and incidence angles, respectively. If the incidence angle from LED is greater than the field of view angle of the photodiode, then in that situation, optical channel gain is zero.

### 2.2 Analytical model of WT-based NHS-OFDM technique for MIMO-VLC system

The proposed  $2 \times 2$  indoor MIMO-VLC system is developed using the NHS-OFDM technique and displayed in Fig. 2. Incoming high-rate digital data has first input to serial to parallel (S/P) block, where digital data is fragmented across several narrowband parallel sub-carriers that are orthogonal to each other. These sub-carriers are then encoded using a conventional digital modulation scheme, i.e., quadrature-amplitude modulation (QAM). After mapping to complex QAM symbols, an inverse discrete WT (IDWT) is executed on frequency-domain sub-carriers to yield the OFDM symbol in the time domain. Full details of

Fig. 1 MIMO-VLC Model Using (a) NImR and (b) ImR.



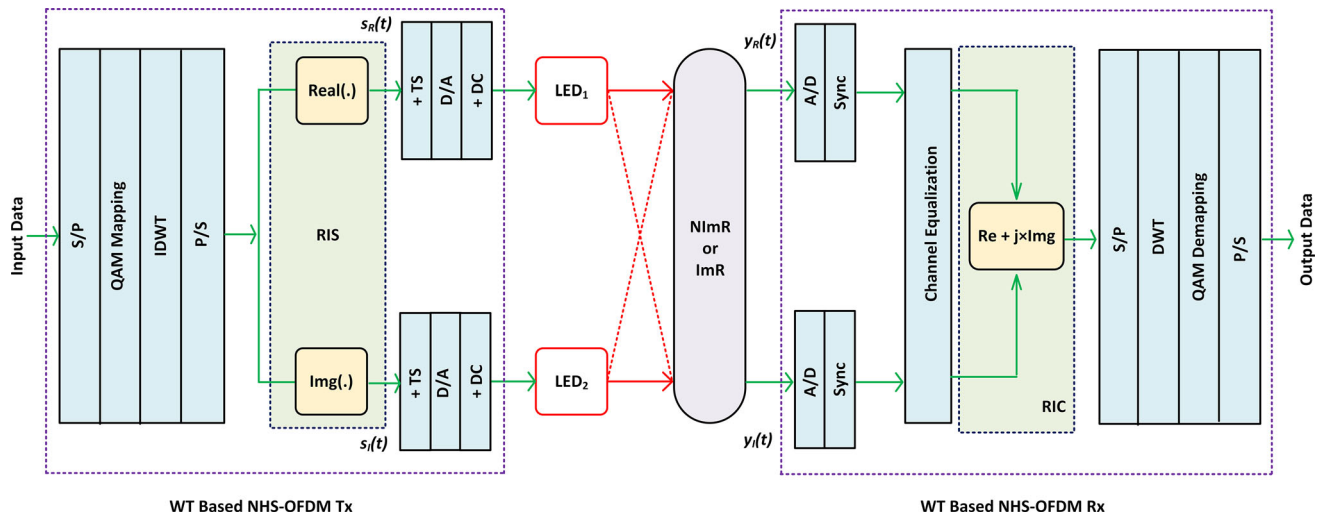


**Fig. 2** Block diagram of  $2 \times 2$  indoor MIMO-VLC system using WT-based NHS-OFDM

IDWT/DWT operation will be available within the next section. Next, a parallel to serial (P/S) block is exploited to alter the OFDM modulated symbols into a single complex modulating waveform.

To make the modulating waveform compatible with LED communication, a real-and-imaginary separator (RIS) is employed in system design that segregates real and imaginary parts of a complex-valued OFDM signal. Hence, two bipolar real-valued analog signals  $s_R(t)$  and  $s_I(t)$  are formed. In these signals, training sequences (TS) are added, and later, the digital signal is converted to an analog signal using the D/A block. Next, to modulate the intensities of two LEDs, a fixed DC value is added individually with bipolar signals that result in unipolar signals. After transmitting the signals  $s_R(t)$  and  $s_I(t)$ , over a free-space optical channel, non-imaging (NImR) or ImR receivers collect the optical signals. Subsequently, receivers yield two signals  $y_R(t)$  and  $y_I(t)$ .

Before passing these signals to the channel estimator, the signals are first transformed back from analog to digital domain using the D/A block. Then time synchronization is achieved by exploiting TS, such that perfect synchronization of sampling clock and OFDM-symbol period is obtained in the receiver(s). In the next step, zero-forcing-based channel equalization is performed to recover the real and imaginary parts of the OFDM signal. Both parts are transformed back to the complex-valued OFDM signal by the use of a real-and-imaginary combiner (RIC). Received complex-valued OFDM waveform is input to S/P block and sub-carriers are transmuted to the frequency domain using DWT operation. Finally, QAM demodulation is executed and the output is produced by combining parallel sub-carriers.

### 2.3 Wavelet analysis

Analysis of non-stationary signals can be done by identifying transitions and discontinuities. As an example, consider a standard FT that isolated the distinct frequency components of a continuous-time domain signal  $s(t)$ . For breakdown, FT practices multifaceted sinusoidal basis functions  $e^{-j\omega t}$  that are infinite and periodic. Consequently, any small interval signal spreads over the entire basis. Contrariwise, the MRA procedure breaks incoming signals over a finite-length basis function, whose essential components are confined in both frequency and time domains. In that way, the MRA technique straightaway edifies the main frequency components, and their presence in time, on which unpredicted changes take place [29].

In general, the continuous WT (CWT) is determined by carrying out the correlation procedure amongst continuous signal  $s(t)$  and scaled form of mother wavelet  $\psi(t)$ . Mathematically [30],

$$CWT(a, \tau) = \frac{1}{|a|} \int s(t)\psi^*\left(\frac{t-\tau}{a}\right)dt \tag{4}$$

where operator  $*$  symbolises complex conjugate,  $a$  signifies a real non-zero scale parameter, while  $\tau$  is translation factor. It is noteworthy that the mother wavelet  $\psi(t)$  must satisfy the admissibility condition, which can be characterized by following mathematical expression [31].

$$c_\psi = \int \frac{|\tilde{\psi}(f)|^2}{|f|} df < \infty \tag{5}$$

where  $\tilde{\psi}(f)$  indicates frequency-domain exemplification of  $\psi(t)$ . Original signal  $s(t)$ , can be reconstructed using an inverse wavelet transform, for which the mathematical expression is as follows [30],



$$s(t) = \frac{1}{c_\psi} \int \int CWT(a, \tau) \frac{1}{\sqrt{|a|}} \psi\left(\frac{t - \tau}{a}\right) \frac{da dt}{a^2} \quad (6)$$

By utilizing the Fourier Parseval theorem, Eq. 4, can be amended as,

$$CWT(a, \tau) = \sqrt{|a|} \int \tilde{s}(f) \tilde{\psi}^*(-af) e^{-j2\pi f \tau} df \quad (7)$$

where  $\tilde{s}(f)$  represents FT of the original signal. From Eq. 7, it can be concluded that CWT is the output of filter banks obtained by dilations/compressions of the mother wavelet. It is remarkable to note that filters acquired by dilating the mother wavelet contribute to low-frequency content of  $s(t)$ , whereas filters associated with compacted forms of mother wavelet offer high-frequency statistics.

The by-hand CWT analysis of signals is a very tedious task, so a discretized form of CWT is used, which is usually designated as discrete wavelet transform (DWT). DWT is a multi-resolution technique whose practical enactment is completed using a dyadic filter bank infrastructure, where an incoming data signal is decomposed into different frequency components using analysis filter banks, and then each frequency component is individually analyzed at specific resolutions according to their scales using synthesis filter banks [32]. Dyadic filter bank structure for digital communication systems is put on display in Fig. 3, where a synthesis-filter bank is engaged at the transmitter side and an analysis-filter bank at the receiver side, respectively.

In DWT, a signal to be analyzed is fed to successive corresponding low-pass  $g[n]$  and high-pass  $h[n]$  filters, which decompose a signal into its approximation/scaling  $c_1[n]$  and detail  $d_1[n]$  coefficients. High-pass filter contents have no noteworthy information and for this reason, are not further decomposed. Nevertheless, the low-frequency contents are further decomposed into two bands. In this manner, the process of decomposition lasts until a reasonable level of information is acquired. The process of

splitting spectrum using a filter band is exhibited in Fig. 4(a), while Mallat’s pyramidal decomposition structure with approximate and detail coefficients is displayed in Figure 4(b). Following relations determine the first level of approximate  $c_1[n]$  and detail  $d_1[n]$  coefficients [33, 34],

$$\begin{aligned} c_1[n] &= \sum_k c_0[k] h[2n - k] \\ d_1[n] &= \sum_k c_0[k] g[2n - k] \end{aligned} \quad (8)$$

where  $c_0[n]$  are expansion coefficients of signal  $s(t)$ . For all frequencies, high-pass and low-pass filters must satisfy the quadrature mirror filter (QMF) condition, i.e., the cumulative sum of individual filter responses is equivalent to unity. Decomposing the signal with QMF filters halves the time-resolution while increasing the frequency resolution by twice. Owing to this, the output signal’s frequency band spans only half the original signal band; hence, one-half of samples are thrown away by a down-sampling operation, deprived of any information loss. The process of decomposition can be continued, and at every level  $l$ , filtering and down-sampling operation halve both samples and frequency band. Therefore, the generic equations for each decomposition level  $l$  of approximate and detail coefficients are formulated as follows [33, 34];

$$\begin{aligned} c_l[n] &= \sum_k c_{l-1}[k] h[2n - k] \\ d_l[n] &= \sum_k c_{l-1}[k] g[2n - k] \end{aligned} \quad (9)$$

Here,  $c_l[k]$  and  $d_l[k]$  are the approximate and detail coefficients at each decomposition level with a resolution  $2^l$ . In comparison to standard FT, WT has less computational complexity because, at each level, a lesser number of samples are handled that amends both time and frequency resolution. Reverse filtering and up-sampling operations reconstruct expansion coefficients  $c_0[n]$  of the input signal [30]:

$$c_0[n] = \sum_k c_1[k] h[2k - n] + d_1[k] g[2k - n] \quad (10)$$

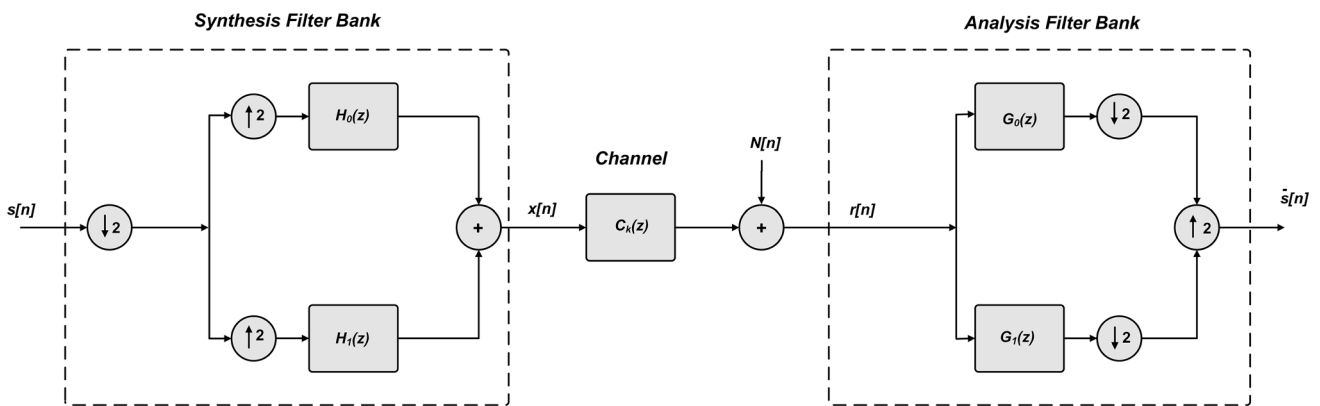
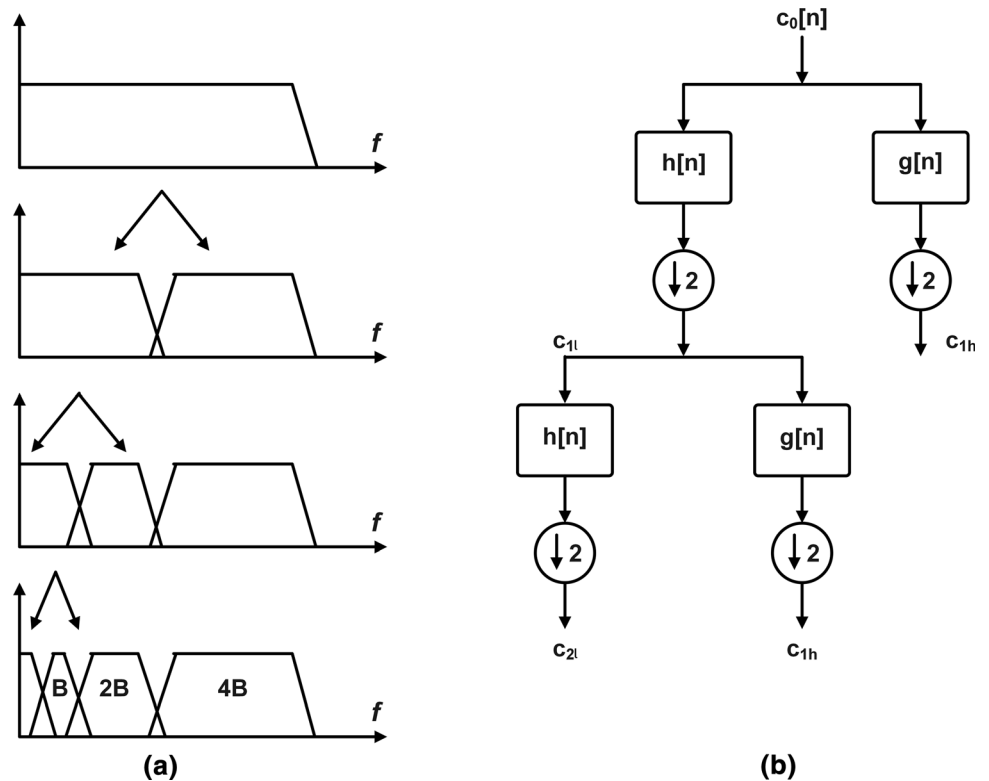


Fig. 3 Filter bank structure

**Fig. 4** Discrete wavelet transform procedure: (a) signal decomposition and (b) Mallat’s pyramidal structure for decomposition



### 3 Closed-form BER expressions for MIMO-VLC system

This section comprehensively gives mathematical calculations for deriving closed-form analytical BER expressions for the proposed MIMO-VLC system using NImR and ImR. It is noteworthy that analytical BER expressions of the traditional FT-based NHS-OFDM system are necessary for the comparative perspective. Therefore, we first derive closed-form BER expressions of it in the presence of LOS link and then associate these expressions with our proposed WT-based NHS-OFDM system (explained in Sect. 2.2).

#### 3.1 Analytical BER derivation of FT-based NHS-OFDM technique for MIMO-VLC system

For analytical BER analysis, ponder that two transmitting LEDs emits data at the same optical power  $P_T$ , while two photodiodes that detect the optical signal also have identical responsivity  $R_O$ . Photodiode responsivity is well-defined as the ratio of produced photo-current to incident optical power, determined in the linear region of response. Notably, responsivity is typically high in a wavelength region, where the photon energy is slightly above the bandgap energy and decreases abruptly in the bandgap region, where the absorption decreases. It is computed using the relation,  $R_O = \eta \frac{e}{h\nu}$ , where  $h\nu$  signifies photon

energy,  $\eta$  indicates quantum efficiency, and  $e$  is the elementary charge. The signal vector communicated in the case of the NHS-OFDM-based MIMO-VLC system is specified by  $s_{NHS} = [s_R \ s_I]^T$ , analogous to complex-valued NHS-OFDM signal,  $s_{NHS}(t) = s_R(t) + j \times s_I(t)$ . Detected/received time-domain optical signal vector  $r_{NHS} = [r_R \ r_I]^T$  is expressed as:

$$r_{NHS} = R_O P_T H_{LOS} s_{NHS} + w_{NHS} \tag{11}$$

where  $H_{LOS}$  is optical channel matrix and  $w_{NHS} = [w_R \ w_I]^T$  indicates real-valued white noise vector. If NImR is employed as a MIMO receiver than  $H_{LOS}$ , turn into Eq. 1, while with ImR,  $H_{LOS}$  becomes Eq. 2. White noise vector is modeled as Gaussian noise with a mean equal to zero, and variance  $\sigma_{FFT}^2$ . Meaningful data from the received signal is recovered by making use of MIMO demultiplexing. To date, myriad MIMO demultiplexing schemes have been reported in the literature, among them ZF scheme is the most popular one. Thanks to the low complexity feature of ZF, current work adopted it for MIMO demultiplexing. ZF is the modified form of the conventional decorrelating equalizer. If the noise term within the received signal is zero, then it completely confiscates the channel effects. However, this could not be an ideal case because noise always exists in the received signal. After carrying out MIMO demultiplexing, the recovered signal can be formulated as,

$$\tilde{s}_{NHS} = \frac{1}{R_{OP_T}} H_{LOS}^{-1} r_{NHS} \tag{12}$$

By replacing  $r_{NHS}$  from Eq. 11, into Eq. 12, and later, by simplification, the recovered signal vector becomes,

$$\begin{aligned} \tilde{s}_{NHS} &= \frac{1}{R_{OP_T}} H_{LOS}^{-1} (R_{OP_T} H_{LOS} s_{NHS} + w_{NHS}) \\ \tilde{s}_{NHS} &= s_{NHS} + \frac{1}{R_{OP_T}} H_{LOS}^{-1} w_{NHS} \end{aligned} \tag{13}$$

Executing multiplication operation between Gaussian variables through any signal does not alter statistics of Gaussian noise, and hence, it remains the same. However, due to  $\frac{1}{R_{OP_T}} H_{LOS}^{-1}$  factor, noise power varies, which can be handle by the use of SNR. At low SNR values, the noise term becomes substantial, and the performance of the ZF equalizer is tainted. On the other hand, at high SNR values, ZF can straightforwardly eliminate the noise term. Because of a given fact, the simplified form of the recovered signal is exhibited as,

$$\tilde{s}_{NHS} = s_{NHS} + w_{NHS} \tag{14}$$

After estimating the signal, the complex-valued NHS-OFDM signal is reconstructed using the following relation.

$$\tilde{s}_{NHS}(t) = \tilde{s}_R(t) + j \times \tilde{s}_I(t) \tag{15}$$

The estimated signals are then transformed by employing FFT. Mathematically,

$$\tilde{S}_{NHS} = S_{NHS} + W_{NHS} \tag{16}$$

where  $S_{NHS} = FFT\{s_{NHS}\}$  and  $W_{NHS} = FFT\{w_{NHS}\} = \frac{1}{\sqrt{N}} \sum_{k=0}^N w_{NHS} e^{-j\frac{2\pi k}{N}}$ , where  $k$  entitles the  $k$ -th sub-carrier. From Eq. 16, it is clear as broad daylight that  $S_{NHS}$  can be efficiently recovered after baseband demodulation, although there is still exists chances of error due to noise term. For this reason, it is necessary to investigate the impact of AWGN on the recovered signal after it has been sent over FT-based filter banks. As mentioned in previous texts, noise is modeled as Gaussian noise, therefore mean  $E\{W_{NHS}\}$  is equal to zero, which makes its power equal to its variance. Noise variance  $\sigma_{FFT}^2$  after FFT operation is formulated as;

$$\sigma_{FFT}^2 = E \left( \left( \frac{1}{\sqrt{N}} \sum_{k=0}^N w_{NHS} e^{-j\frac{2\pi k}{N}} \right)^2 \right) \tag{17}$$

Next, by making use of results given in Eq. 13, the SNR with a NImR is indicated by,

$$SNR_{NHS}^{NImR} = (R_{OP_T})^2 \frac{2(h_{11}h_{22} - h_{12}h_{21})^2}{(h_{21}^2 + h_{22}^2)\sigma_{FFT_R}^2 + (h_{11}^2 + h_{12}^2)\sigma_{FFT_I}^2} \tag{18}$$

where  $\sigma_{FFT_R}^2$  and  $\sigma_{FFT_I}^2$  are variances of the white noise vector  $w_{NHS} = [w_R \quad w_I]^T$ . When ImR is used for MIMO signal reception, the channel gains  $h_{11}$  and  $h_{22}$  turn out to be zero, and SNR for the NHS-OFDM signal is specified by,

$$SNR_{NHS}^{ImR} = (R_{OP_T})^2 \frac{2(h_{12}h_{21})^2}{h_{21}^2 \sigma_{FFT_R}^2 + h_{12}^2 \sigma_{FFT_I}^2} \tag{19}$$

Analytical BER expression for M-ary rectangular QAM over an AWGN channel can be derived using a standard relation [35]:

$$BER_{M-QAM} = \frac{2(\sqrt{M} - 1)}{\sqrt{M} \log_2(M)} Q \left( \sqrt{\frac{3 SNR_{NHS}}{2(M - 1)}} \right) \tag{20}$$

where  $Q(\cdot)$  in the above relation represents Q-function. By substituting SNRs of NHS-OFDM obtained in Eq. 18, and 19, to Eq. 20, yields the BER expressions.

$$\begin{aligned} BER_{NHS}^{NImR} &= \frac{2(\sqrt{M} - 1)}{\sqrt{M} \log_2(M)} Q \left( \sqrt{\frac{3 (R_{OP_T})^2 \frac{2(h_{11}h_{22} - h_{12}h_{21})^2}{(h_{21}^2 + h_{22}^2)\sigma_{FFT_R}^2 + (h_{11}^2 + h_{12}^2)\sigma_{FFT_I}^2}}{2(M - 1)}} \right) \\ BER_{NHS}^{ImR} &= \frac{2(\sqrt{M} - 1)}{\sqrt{M} \log_2(M)} Q \left( \sqrt{\frac{3 (R_{OP_T})^2 \frac{2(h_{12}h_{21})^2}{h_{21}^2 \sigma_{FFT_R}^2 + h_{12}^2 \sigma_{FFT_I}^2}}{2(M - 1)}} \right) \end{aligned} \tag{21}$$

### 3.2 Analytical BER derivation of WT-based NHS-OFDM technique for MIMO-VLC system

From discussions in Sect. 2.3, complex sinusoids of FFT are substituted with QMF filter pair. Consequently, the noise term occurring on each sub-carrier of the NHS-OFDM is changed. For this reason, we first determine noise variances that help us in deriving BER expressions for the WT-based NHS-OFDM technique for the MIMO-VLC system. Estimated complex-valued NHS-OFDM signal (Eq. 15) is applied to wavelet filter bank using low-pass and high-pass filters at their respective decomposition levels. In the first level, detailed coefficients at the output of the high-pass filter are obtained, and these coefficients are not decomposed further. Similarly, approximate coefficients are available at the output of the low-pass filter, and at the second level, they are further broken up into fundamental approximate and detailed coefficients. It is imperative to note that this process is repeated for all



successive levels in DWT. More detailed discussions can be reviewed from [36]. While the following relationship indicates the output produced by the wavelet filter bank before QAM demodulation,

$$\tilde{S}_{NHS} = S_{NHS} + W_{NHS} \tag{22}$$

where  $S_{NHS}$  and  $W_{NHS}$  depicts DWT of the complex-valued NHS-OFDM signal and noise term, respectively. The output signal is obtained by applying a circular convolution operation between the received signal and the impulse response of wavelet filters. Initially, the received signal is down-sampled via a factor of 2 and later, at the first level, filtered utilizing  $g[n]$  and  $h[n]$ . After first level decomposition, the approximate and detailed coefficients are approximated in terms of channel noise as follows [36],

$$\begin{aligned} c_{1n}[n] &= (w_{NHS} \otimes h[n]) \downarrow 2 \\ d_{1n}[n] &= (w_{NHS} \otimes g[n]) \downarrow 2 \end{aligned} \tag{23}$$

where  $w_{NHS}$  indicates the  $n^{th}$  noise component, which is an independent and identically distributed Gaussian variable with a mean of zero. Therefore, the received DWT processed signal is handled in the context of noise variance. Noise variance  $\sigma_{DWT}^2$ , for the first level of decomposition, is formulated as [36],

$$\begin{aligned} \sigma_{DWT_{c1}}^2 &= \delta_{DWT}^2 \sum_{\alpha} (h_{\alpha}^N)^2 \\ \sigma_{DWT_{d1}}^2 &= \delta_{DWT}^2 \sum_{\alpha} (g_{\alpha}^N)^2 \end{aligned} \tag{24}$$

where  $\delta_{DWT}^2$  corresponds to channel noise at the first level of decomposition while  $h_{\alpha}^N$  and  $g_{\alpha}^N$  are downsampled and convolved forms of  $g[n]$  and  $h[n]$  filters, respectively. Similarly, noise variances at the second level of decomposition for high-pass  $\sigma_{DWT_{c2}}^2$  and low-pass  $\sigma_{DWT_{d2}}^2$  filters are written in the convolved form as [36],

$$\begin{aligned} \sigma_{DWT_{c2}}^2 &= \delta_{DWT}^2 \sum_{\alpha} (h_{(\alpha(m,N))} \odot h_k^{\frac{N}{2}})^2 \\ \sigma_{DWT_{d2}}^2 &= \delta_{DWT}^2 \sum_{\alpha} (g_{(\alpha(m,N))} \odot g_k^{\frac{N}{2}})^2 \end{aligned} \tag{25}$$

Accordingly, noise variance is the sum of individual variances resulted from each DWT branch. Mathematically [36],

$$\sigma_{DWT}^2 = \sigma_{DWT_{dMn}}^2 + \sum_{k=1}^M \sigma_{DWT_{ckn}}^2 \tag{26}$$

From the abovementioned Eq. 26, it is obvious as broad daylight that noise variance of the channel at the output of the DWT filter bank is a combination of noise variance of the low-pass filter of  $M$ -th branch and the summed values of noise variance of all the high-pass filter outputs of  $M$  branches.

## 4 Simulation setup and discussions on numerical results

This section addresses the simulation setup for the considered  $2 \times 2$  MIMO-VLC system model and later presents the numerical investigation of conventional and proposed techniques used to develop the MIMO-VLC systems. MATLAB simulator is employed for the empirical investigation, where simulation packages for both conventional and proposed techniques are developed, using MATLAB script (m-files) and MATLAB built-in functions (such as ifft, fft, idwt, and dwt, etc.). As analytical BER expressions using NiM and ImR for the FT-based HS-OFDM technique have already been derived in [22], we borrow these mathematical expressions and use them as a benchmark. Furthermore, the analytical BER of NHS-OFDM-based MIMO-VLC systems is compared with the BER of the HS-OFDM-based MIMO-VLC system.

Monte-Carlo simulations have been utilized to validate analytical BER curves using the mathematical formulas obtained in Sect. 3. To ensure reasonable comparisons, optical power emanating by the luminaries in each MIMO-VLC system is precisely fixed, and error rates are carefully estimated at the receiver side, keeping in view SNR. The transmitter of each MIMO-VLC technique generates  $10^5$  OFDM (HS-OFDM and NHS-OFDM) modulated symbols. Rendering to the simulation parameters recorded in Table 1, both HS-OFDM and NHS-OFDM techniques produce equiprobable binary information, on which 16-ary square QAM complex mapping is applied, while the IFFT/FFT and IDWT/DWT sizes are fixed at 64. Additionally, the number of data sub-carriers in both HS-OFDM and NHS-OFDM techniques is set to 63. Both VLC transmitters and receivers are synchronized with each other while the perfect knowledge of the channel is available at the receiver. Wavelet analysis is performed using the Haar wavelet.

The crucial simulation parameters for the indoor MIMO-VLC system setup are enumerated in Table 2. A vacant room with dimensions  $3m \times 3m \times 2.5m$  is taken into consideration where two luminaries are oriented on the rooftop, while they typically emit optical intensity in the downward direction. These two luminaries are capable of delivering data and illumination simultaneously. Each luminary is made up of 16 LEDs arranged in an array of  $4 \times 4$  patterns, while the luminaries remain positioned at  $(-0.5, 0, 2.5)$  and  $(0.5, 0, 2.5)$  on the plastered ceiling, respectively. The LEDs within the luminary emanates monochromatic white light having a Lambertian radiation pattern and transforms the electrical signal into the optical signal. Based on the modulated signal, each luminary is either OFF for zero-intensity level or radiate light by a

**Table 1** Key simulation parameters for OFDM techniques based indoor MIMO-VLC systems

Key parameters	FT-HS-OFDM	WT-HS-OFDM	FT-NHS-OFDM	WT-NHS-OFDM
Number of luminaries	2	2	2	2
Number of VLC receivers	2	2	2	2
Number of OFDM symbols	$10^5$	$10^5$	$10^5$	$10^5$
Complex modulation	16-ary square QAM	16-ary square QAM	16-ary square QAM	16-ary square QAM
Data sub-carriers	63	63	63	63
Total sub-carriers	64	64	64	64
Size of cyclic prefix	$1/4^{th}$	Not required	$1/4^{th}$	Not required
OFDM symbol size	80 samples	64 samples	80 samples	64 samples
Wavelet family	Not required	Haar	Not required	Haar
Channel	VLC-LOS	VLC-LOS	VLC-LOS	VLC-LOS
Noise type	AWGN	AWGN	AWGN	AWGN
SNR range	0–26 dB	0–26 dB	0–26 dB	0–26 dB
Equalizer	Zero-forcing	Zero-forcing	Zero-forcing	Zero-forcing

**Table 2** Parameters for the indoor MIMO-VLC system setup

Set up parameters	Value(s)
Dimensions of room (length $\times$ width $\times$ height)	3m $\times$ 3m $\times$ 2.5m
Luminaries placement	(-0.5, 0, 2.5) (0.5, 0, 2.5)
Number of LEDs in a luminary	16 (4 $\times$ 4)
Distance between LEDs within a luminary	1.5cm
Workbench height	0.5m
LED's Semi-angle at half-power	$15^0$
Modulation index	0.3
Optical filter gain	1
Lens type	NImR, ImR (convex imaging lens)
Responsivity of photodiode	1 A/W
Operative area of the photodiode	1 $cm^2$
Gain of optical lens	1
Field of view angle of a photodiode	$15^0$
Spacing between two VLC receivers	0.3 m

certain intensity level. Within a luminary, the LEDs are placed 1.5 cm apart, resulting in an overall increase in optical intensity.

Keeping in view the specific placement of luminaries, the VLC receivers are oriented on a workbench at the height of 0.5 m above the floor. The receivers are placed on the receiving plane such that they are vertically focused on the rooftop and creates a LOS link. On top of that, it is worth noticing, VLC receivers are also fortified with the NImR and ImR. NImR is developed using a normal optical lens and photodiode, while an ImR contains a convex imaging lens and photodiode. The location of the photodiode beneath the convex imaging lens is set in such a way

that it receives the optical signal from the centroid of the aperture of the lens, and the lens focused the optical signals onto the photodiode such that the image of the optical signal appears as a spot. The active area of each photodiode is assumed to be 1  $cm^2$ , while the spacing between the two receivers is fixed to 0.3 m. By making use of European Union Project OMEGA as the standard for the LOS link, the semi-angle at half-power of LED and field of view of the photodiode are each chosen as  $15^0$  respectively. The modulation index is selected to be 0.3, while the responsivity of the photodiode is equal to 1 A/W. Likewise, the gain of optical filter and lens are each deliberated as 1.

### 4.1 BER performance assessment

Primarily, the BER performance of conventional and proposed modulation techniques for MIMO-VLC systems with NImR is investigated for targeted BER of  $10^{-4}$ . The detailed analytical and simulated BER results are exhibited in Fig. 5, where markers indicate the analytical results while solid lines imply the simulated results. By inspecting the presented results, it can be pointed out that the simulated results are in agreement with the analytical results, validating the theoretical calculations performed in Sect. 3. Over and above, it is also deduced that the proposed WT-based NHS-OFDM modulation technique for the MIMO-VLC system outperforms all other conventional modulation techniques. Unlike the conventional FT-based HS-OFDM technique, the FT-based NHS-OFDM technique realizes an SNR gain of almost 4.4 dB. However, the error performance of HS-OFDM can be amended by substituting FT with the WT. From outcomes, this performance improvement is about 1.1 dB. Likewise, the error performance of FT-based NHS-OFDM is further boosted by engaging wavelets. It is found that the overall error performance of the WT-based NHS-OFDM technique in common is 1.4 dB superior to the FT-based NHS-OFDM technique.

Next, simulations are also carried out in MATLAB for conventional and proposed modulation techniques with ImR, and the practical outcomes are strikingly illustrated in Fig. 6. Analogous to Fig. 5, specific markers typically

provide the analytical results, whereas solid lines prominently display simulated results. For ImR-based BER results, it is clear that simulated results closely overlap with the analytical results. Significantly, the error performance of proposed NHS-OFDM-based modulating schemes for the MIMO-VLC system is also assessed for targeted BER of  $10^{-4}$  and compared with the HS-OFDM-based MIMO-VLC system. In this place, in Fig. 6, it is apparent that again the performance of the FT-based NHS-OFDM technique outperforms the FT-based HS-OFDM technique by getting the gain of approximately 4.2 dB. Despite the use of WT with the HS-OFDM technique, the error performance is improved to some extent, but this performance still deteriorates when compared with the FT-based NHS-OFDM technique. It can be recognized from the results that the error performance of the WT-based HS-OFDM technique is 2.3 dB better than its counterpart technique. As BER results for the HS-OFDM technique achieve significant improvement by realizing the wavelets, therefore, wavelets are also incorporated with the novel NHS-OFDM technique. From comparative analysis, it could be confirmed that the WT-based NHS-OFDM technique accomplishes 2 dB enhanced results than the FT-based NHS-OFDM technique.

A comparative analysis of BER curves is also performed for both conventional and proposed modulating techniques with and without ImR, which are presented in Figs. 5 and 6. By comparing BER curves for targeted BER of  $10^{-4}$ , the FT-based HS-OFDM technique with ImR performs

**Fig. 5** Analytical versus simulated BER performance comparison of conventional and proposed techniques for the  $2 \times 2$  MIMO-VLC system using NImR

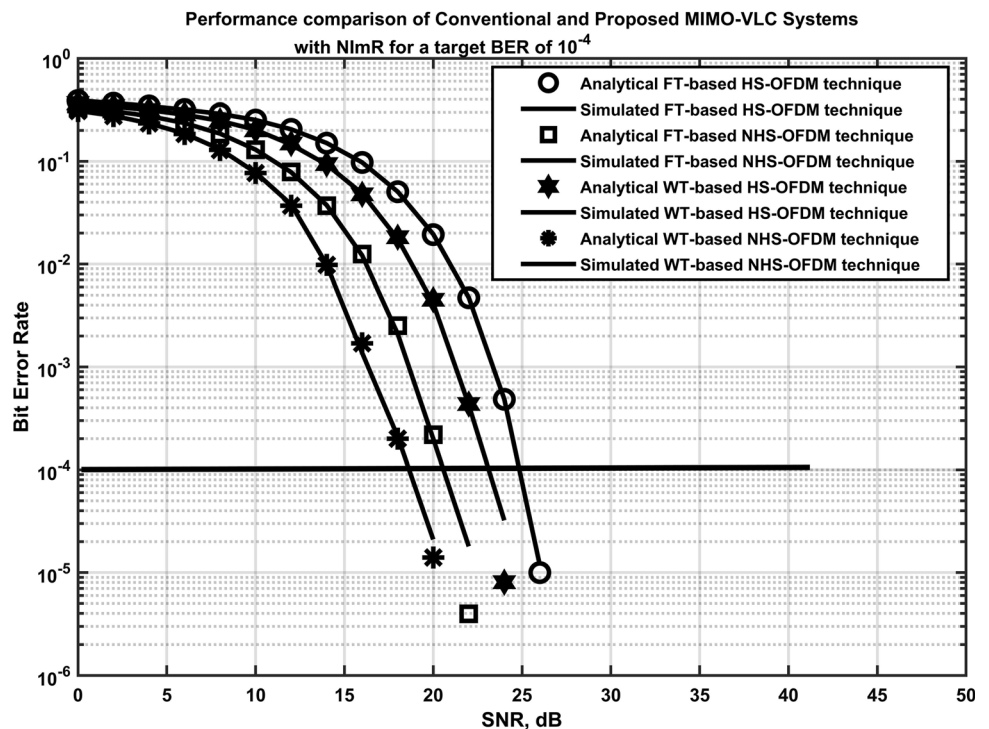
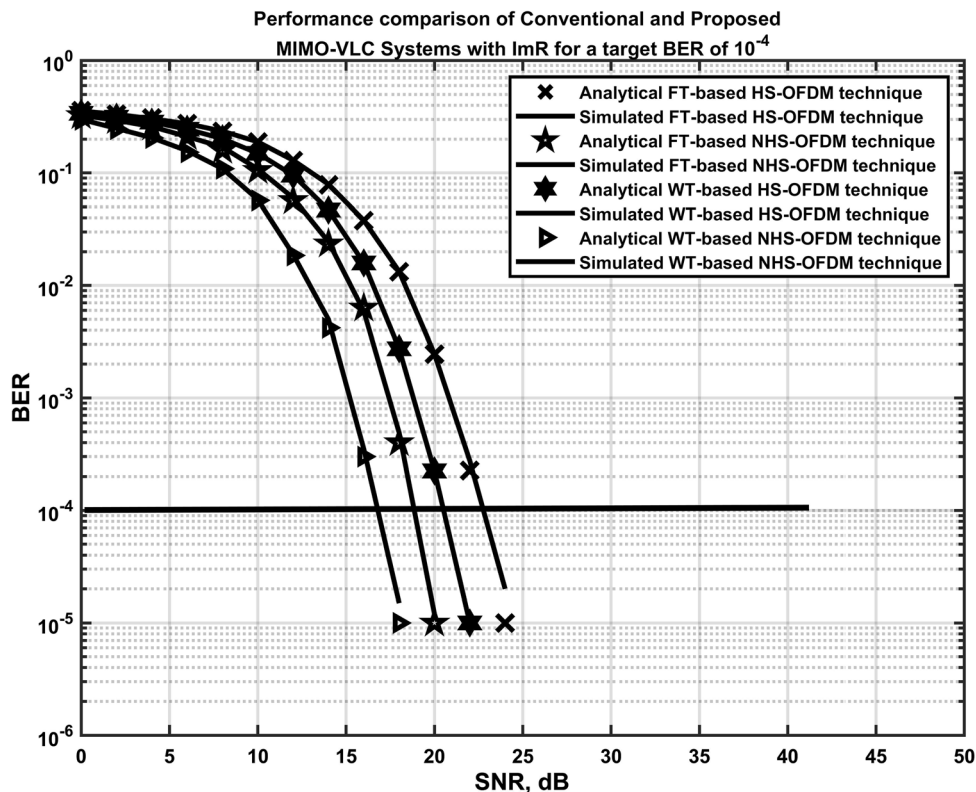


**Fig. 6** Analytical versus simulated BER performance comparison of conventional and proposed techniques for the  $2 \times 2$  MIMO-VLC system using ImR



approximately 1.5 dB better than the NImR-based technique. When WT is used instead of FT, the error performance of the HS-OFDM technique with ImR is much better and accomplishes a coding gain of approximately 2.3 dB. A similar BER profile is also witnessed for the WT-based NHS-OFDM technique using ImR. From the analysis of Figs. 5 and 6, it is concluded that for a  $2 \times 2$  MIMO indoor VLC system, the WT-based NHS-OFDM scheme with ImR is the best choice. This is because the BER profile of the WT-based NHS-OFDM technique is exceptional to BER profiles of other techniques. Further, it is imperative to state here that the overall performance of the MIMO systems can be improved just by extending the system for more transmitter(s)/receiver(s) pairs, which is contradictory to the proposed WT-based NHS-OFDM technique for indoor MIMO-VLC system. This is because the transmission of real and imaginary parts can only require two separate antennas, i.e., one transmit antenna for the real part of the NHS-OFDM signal and the second for the imaginary part.

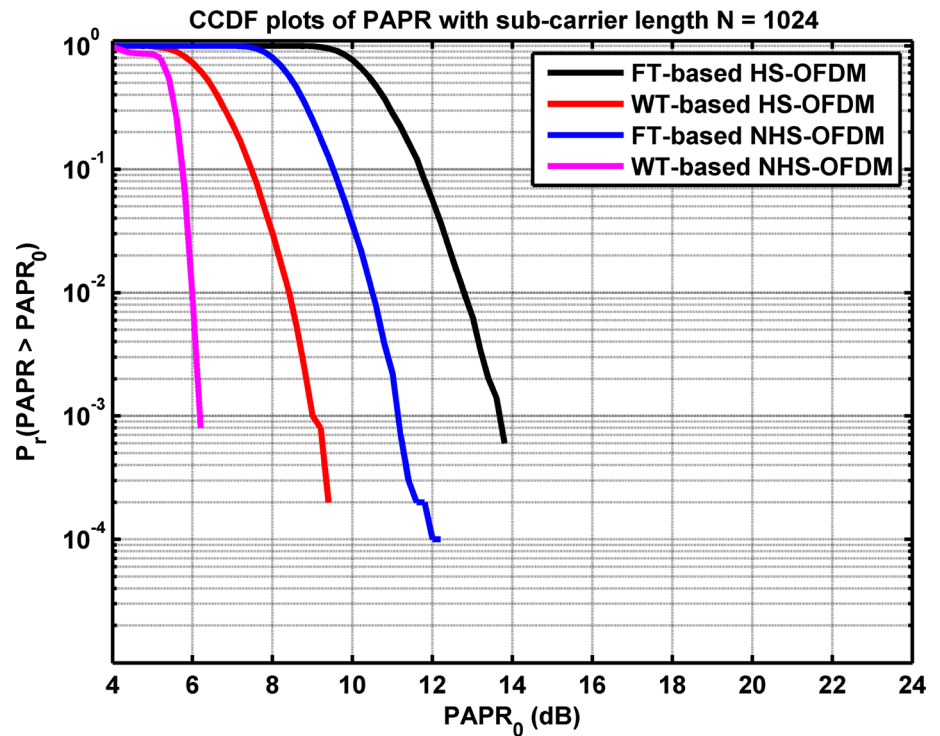
#### 4.2 Computational complexity of MIMO-VLC transceiver

Computational complexity (CC) is a very crucial metric that performs a pivotal role in designing an OFDM-based

MIMO system. From [22], a closer look at the schematic diagram for  $2 \times 2$  MIMO-VLC system using FT-based HS-OFDM technique reveals that two pairs of transmitters/receivers are needed to properly implement the MIMO transceiver. In each transmitter, the HS-OFDM modulating technique is implemented individually. As a result, two N-point IFFT/FFT modules are required to efficiently convert subcarriers from frequency-domain to time-domain and vice versa. However, for the FT-based NHS-OFDM technique, we modulate binary data exploiting the RF-based OFDM technique and then segregate real and imaginary parts to transmit them from a pair of transmitters. For this reason, a single IFFT/FFT module is enforced for the NHS-OFDM technique, which reduces both the cost and CC of the MIMO-VLC system.

It is necessary to mention here that to obtain the real-valued OFDM modulating waveform, HS is carrying out, which increases IFFT/FFT size by two times. CC regarding the number of additions and multiplications resulted from the HS-based OFDM system for a single transmitter/receiver pair is represented by  $O(2N \log(2N))$  [17], where  $N$  shows the length of the sub-carrier. However, CC of the proposed FT-based NHS-OFDM technique for two transmitter/receiver pairs is formulated as  $O(N \log(N))$  [17]. The formula for computing the percentage change in complexity is expressed by the following relationship,

**Fig. 7** CCDF comparison of conventional and proposed techniques for the  $2 \times 2$  MIMO-VLC system



$$\% \text{ change in complexity} = \frac{| \text{complexity of conventional scheme} - \text{complexity of proposed scheme} |}{\text{complexity of conventional scheme}} \times 100\% \tag{27}$$

To ensure fair comparisons, the size of subcarriers is 64. Using Eq. 27, CC of the FT-based NHS-OFDM technique requires about 57% less than the FT-based HS-OFDM technique, which could also be verified from [17]. Contrariwise, the CC for a discrete WT-based OFDM system is characterized as  $O(N)$  related to the number of additions and multiplications [19, 37]. Moreover, consider that length of the low-pass and high-pass filters associated with  $N$  is negligible. Using Eq. 27, CC of the WT-based NHS-OFDM technique for the MIMO-VLC system is 44% less than the corresponding FT-based NHS-OFDM technique. While this CC is 76% lower than the conventional FT-based HS-OFDM technique. Hence, the proposal of incorporating wavelets in the OFDM-based MIMO-VLC system has proven to be a very good solution.

### 4.3 PAPR profile

Having discussed BER profiles and CC of conventional and proposed techniques for the MIMO-VLC system, let us now turn to the PAPR profile. In OFDM-based communication systems, PAPR remains the utmost concern that needs to be reduced significantly. At each antenna of the standard MIMO OFDM system, PAPR embodies the ratio of maximum power to the average power of an OFDM

signal, which is associated with the following mathematical expression,

$$PAPR = \frac{\max [ |s(n)|^2 ]}{E [ |s(n)|^2 ]} \quad \text{for} \quad 0 \leq n \leq NL - 1 \tag{28}$$

where  $E\{.\}$  indicates expected value of the signal while  $L$  signifies the oversampling factor. Note that the PAPR of discretized signal  $s(n)$  is not comparable to PAPR of a continuous signal  $s(t)$ , since  $s(n)$  may not have contained all the peaks of  $s(t)$ . Generally, to address this issue, oversampling factor is utilized. It has been publicized in [38] that an oversampling factor of  $L = 4$  is appropriate to relate PAPR results of discrete-time signals with the continuous-time signals.

The CCDF is the parameter that gives statistics about the percentage of OFDM signals that have a PAPR value above a certain threshold. Primarily, it is a probability that typically indicates the PAPR of an OFDM symbol exceeds the given specific value  $\gamma$ . Mathematically, CCDF is represented as,

$$CCDF(N, \gamma) = \Pr \{ PAPR > \gamma \} = 1 - (1 - e^{-\gamma})^N \tag{29}$$

where  $N$  epitomizes the sub-carriers of the OFDM waveform. In MIMO systems, PAPR is determined by calculating the maximum PAPR from PAPR of all parallel transmitting antennas. PAPR for the MIMO system is formulated as,



$$PAPR_{MIMO} = \max\{PAPR_l\} \quad (30)$$

where  $l = 1, 2, \dots, N_T$  and  $N_T$  are the number of transmit antennas. Figure 7 displays PAPR profiles for conventional and proposed techniques for targeted CCDF of  $10^{-3}$ . PAPR of conventional FT-based HS-OFDM and NHS-OFDM techniques are 13.7 and 11.1 dB, correspondingly. Comparative analysis of both techniques shows that the NHS-OFDM achieves a reduction gain of 2.6 dB. While PAPR performance of WT-based HS-OFDM is also computed and compared with the PAPR of WT-based NHS-OFDM. With the fixed CCDF of  $10^{-3}$ , PAPR of the WT-based NHS-OFDM method is about 2.8 dB better than that of the WT-based HS-OFDM technique. However, when the PAPR of WT-based HS-OFDM is compared with its counterpart FT-based HS-OFDM, a PAPR reduction of 4.7 dB is observed. A similar trend of PAPR improvement (about 4.9 dB) is also sighted when comparing WT-based NHS-OFDM with FT-based NHS-OFDM. This PAPR improvement is resulted because of pulse shaping inherently offered by the wavelets.

## 5 Concluding remarks

This research article has proposed and analytically verified a novel WT-based NHS-OFDM technique for  $2 \times 2$  MIMO-VLC system using ImR that has appeared to be a strong candidate in Future Wireless Networks (FWNs). Work presents closed-form analytical BER expressions for MIMO-VLC systems developed using conventional and proposed techniques with NImR and ImR. Analytical results have exhibited that the proposed technique with ImR has very low CC while performance-wise, it also performs better when compared to conventional techniques. The CC of the suggested scheme is approximately 44% less than the conventional one. Additionally, the simulated results agreed with the analytical results, which shows the validity of the theoretical analysis. Wavelet transforms are widely used for pulse-shaping because they reduce both ISI and ICI in the system. Hence, usage of cyclic prefix is also omitted in classical OFDM system design that somewhat enhances the spectral efficiency. Moreover, without incorporating any reduction technique, wavelets also exhibit reduced PAPR results. In the future, the proposed WT-based NHS-OFDM technique for the MIMO-VLC system will be implemented by making use of cost-effective hardware components and tested at least for multi-media communication.

## References

- Kumar, A., & Gupta, M. (2018). A review on activities of fifth generation mobile communication system. *Alexandria Engineering Journal*, 57(2), 1125–1135.
- Chowdhury, M. Z., Hossan, M. T., Islam, A., & Jang, Y. M. (2018). A comparative survey of optical wireless technologies: Architectures and applications. *IEEE Access*, 6, 9819–9840.
- Shafi, M., Molisch, A. F., Smith, P. J., Haustein, T., Zhu, P., De Silva, P., Tufvesson, F., Benjebbour, A., & Wunder, G. (2017). 5G: A tutorial overview of standards, trials, challenges, deployment, and practice. *IEEE Journal on Selected Areas in Communications*, 35(6), 1201–1221.
- Zhang, D., Zhou, Z., Mumtaz, S., Rodriguez, J., & Sato, T. (2016). One integrated energy efficiency proposal for 5G IoT communications. *IEEE Internet of Things Journal*, 3(6), 1346–1354.
- Ibhaze, A. E., Orukpe, P. E., & Edeko, F. O. (2020). High capacity data rate system: A review of visible light communication technology. *Journal of Electronic Science and Technology*, 18(3), 100055.
- Garber, L. (2011). Turning on the lights for wireless communications. *Computer*, 44(11), 11–14.
- Elgala, H., Mesleh, R., & Haas, H. (2011). Indoor optical wireless communication: potential and state-of-the-art. *IEEE Communications Magazine*, 49(9), 56–62.
- Grobe, L., Paraskevopoulos, A., Hilt, J., Schulz, D., Lassak, F., Hartlieb, F., Kottke, C., Jungnickel, V., & Langer, K. D. (2013). High-speed visible light communication systems. *IEEE Communications Magazine*, 51(12), 60–66.
- Le Minh, H., Brien, D., Faulkner, G., Zeng, L., Lee, K., Jung, D., Oh, Y., & Won, E. T. (2009). 100-Mb/s NRZ visible light communications using a postequalized white LED. *IEEE Photonics Technology Letters*, 21(15), 1063–1065.
- Afgani, M. Z., Haas, H., Elgala, H., & Knipp, D. (2006, March). Visible light communication using OFDM. In 2<sup>nd</sup> International Conference on Testbeds and Research Infrastructures for the Development of Networks and Communities, 2006. TRIDENTCOM 2006. (pp. 6-pp). IEEE.
- Yeh, C. H., Chen, H. Y., Chow, C. W., & Liu, Y. L. (2015). Utilization of multi-band OFDM modulation to increase traffic rate of phosphor-LED wireless VLC. *Optics Express*, 23(2), 1133–1138.
- Wu, L., Zhang, Z., Dang, J., & Liu, H. (2014). Adaptive modulation schemes for visible light communications. *Journal of Lightwave Technology*, 33(1), 117–125.
- Hsu, C. W., Chow, C. W., Lu, I. C., Liu, Y. L., Yeh, C. H., & Liu, Y. (2016). High speed imaging  $3 \times 3$  MIMO phosphor white-light LED based visible light communication system. *IEEE Photonics Journal*, 8(6), 1–6.
- Khalid, A., Asif, H. M., Mumtaz, S., Al Otaibi, S., & Konstantin, K. (2019). Design of MIMO-visible light communication transceiver using maximum rank distance codes. *IEEE Access*, 7, 89128–89140.
- Armstrong, J., & Lowery, A. J. (2006). Power efficient optical OFDM. *Electronics Letters*, 42(6), 370–372.
- Moreolo, M. S., Muñoz, R., & Junyent, G. (2010). Novel power efficient optical OFDM based on Hartley transform for intensity-modulated direct-detection systems. *Journal of Lightwave Technology*, 28(5), 798–805.
- Barrami, F., Le Guennec, Y., Novakov, E., Duchamp, J. M., & Busson, P. (2013, October). A novel FFT/IFFT size efficient technique to generate real time optical OFDM signals compatible with IM/DD systems. In 2013 European microwave conference (pp. 1247-1250). IEEE.

18. Adnan, A., Liu, Y., Chow, C. W., & Yeh, C. H. (2020). Demonstration of non-Hermitian symmetry (NHS) serial-complex-valued orthogonal frequency division multiplexing (SCV-OFDM) for white-light visible light communication (VLC). *OSA Continuum*, 3(5), 1163–1168.
19. Khalid, A. (2020). Implementation of wavelet transform based non-Hermitian symmetry OFDM for indoor VLC system using Raspberry Pi. *Journal of Optical Communications*.
20. Safari, M., & Uysal, M. (2008). Do we really need OSTBCs for free-space optical communication with direct detection? *IEEE Transactions on Wireless Communications*, 7(11), 4445–4448.
21. Deng, P., & Kavehrad, M. (2017). Software defined adaptive MIMO visible light communications after an obstruction. In Optical Fiber Communication Conference, OSA Technical Digest (online) (Optical Society of America, 2017) (pp. Th1E-5). Optical Society of America.
22. Chen, C., Zhong, W. D., & Wu, D. (2017). Non-Hermitian symmetry orthogonal frequency division multiplexing for multiple-input multiple-output visible light communications. *Journal of Optical Communications and Networking*, 9(1), 36–44.
23. Aldababseh, M., & Jamoos, A. (2014). Estimation of FBMC/OQAM fading channels using dual Kalman filters. *The Scientific World Journal*, 2014.
24. Jayaprakash, A., & Reddy, G. R. (2015). Discrete ambiguity function based analysis of filter bank multicarrier systems. *IETE Technical Review*, 32(5), 330–346.
25. Sarwa, S., Singh, H., Agrawal, S., & Sohi, B. S. (2018). Design of a novel hybrid intercarrier interference mitigation technique through wavelet implication in an OFDM system. *Digital Communications and Networks*, 4(4), 258–263.
26. Zeng, L., Brien, D. C., Le Minh, H., Faulkner, G. E., Lee, K., Jung, D., Oh, Y., & Won, E. T. (2009). High data rate multiple input multiple output (MIMO) optical wireless communications using white LED lighting. *IEEE Journal on Selected Areas in Communications*, 27(9), 1654–1662.
27. Sushanth, K. S., & Chockalingam, A. (2018, June). Performance of imaging receivers using convex lens in indoor MIMO VLC systems. In 2018 IEEE 87<sup>th</sup> Vehicular Technology Conference (VTC Spring) (pp. 1–5). IEEE.
28. Komine, T., & Nakagawa, M. (2004). Fundamental analysis for visible-light communication system using LED lights. *IEEE Transactions on Consumer Electronics*, 50(1), 100–107.
29. Cincotti, G., Moreolo, M. S., & Neri, A. (2005). Optical wavelet signals processing and multiplexing. *EURASIP Journal on Advances in Signal Processing*, 2005(10), 1–10.
30. Mallat, S. G. (2009). A theory for multiresolution signal decomposition: the wavelet representation. In *Fundamental Papers in Wavelet Theory* (pp. 494–513). Princeton University Press.
31. Polikar, R., Topalis, A., Green, D., Kounios, J., & Clark, C. M. (2007). Comparative multiresolution wavelet analysis of ERP spectral bands using an ensemble of classifiers approach for early diagnosis of Alzheimer's disease. *Computers in Biology and Medicine*, 37(4), 542–558.
32. Baig, S., Asif, H. M., Umer, T., Mumtaz, S., Shafiq, M., & Choi, J. G. (2018). High data rate discrete wavelet transform-based PLC-VLC design for 5G communication systems. *IEEE Access*, 6, 52490–52499.
33. Dickenson, R. J., & Ghassemlooy, Z. (2004). BER performance of 166 Mbit/s OOK diffuse indoor IR link employing wavelets and neural networks. *Electronics Letters*, 40(12), 753–755.
34. Rajbhandari, S., Ghassemlooy, Z., & Angelova, M. (2009). Effective denoising and adaptive equalization of indoor optical wireless channel with artificial light using the discrete wavelet transform and artificial neural network. *Journal of Lightwave Technology*, 27(20), 4493–4500.
35. Vitthaladevuni, P. K., Alouini, M. S., & Kieffer, J. C. (2005). Exact BER computation for cross QAM constellations. *IEEE Transactions on Wireless Communications*, 4(6), 3039–3050.
36. Baig, S., Ali, U., Asif, H. M., Khan, A. A., & Mumtaz, S. (2019). Closed-form BER expression for Fourier and wavelet transform-based pulse-shaped data in downlink NOMA. *IEEE Communications Letters*, 23(4), 592–595.
37. Khan, A., & Shin, S. Y. (2018). Wavelet OFDM-based non-orthogonal multiple access downlink transceiver for future radio access. *IETE Technical Review*, 35(1), 17–27.
38. Jiang, T., & Wu, Y. (2008). An overview: Peak-to-average power ratio reduction techniques for OFDM signals. *IEEE Transactions on Broadcasting*, 54(2), 257–268.

**Publisher's Note** Springer Nature remains neutral with regard to jurisdictional claims in published maps and institutional affiliations.



**Arslan Khalid** received the Bachelor's and Master's degrees in electrical engineering from the COMSATS University Islamabad, Lahore campus, Pakistan, in 2012 and 2016, respectively. Mr. Khalid is currently pursuing his Ph.D. Degree from the School of Information, Computer, and Communication Technology (ICT), Sirindhorn International Institute of Technology Thammasat University, Thailand. He has more than five years of the

optical wireless industry and academic experience and has published several papers in well-reputed Journals and International Conferences. In 2017, Mr. Khalid had joined the Department of Electrical Engineering, The University of Lahore, Pakistan as a Lecturer. From 2012 to 2017, he was with the Department of Electrical and Computer Engineering, COMSATS University Islamabad, Lahore campus, Pakistan. His research interests include communication theory, computer networks, wireless communication systems, visible light communication, Multicarrier modulation techniques such as OFDM and its variants, Wavelets and Wavelet transforms, Wavelet Transform based multi-carrier modulation techniques, Code Division Multiple Access (CDMA) technology, Software Defined Radio (SDR), MIMO Systems such as Repetition Coding, Space-Time Block Coding (STBC), Spatial Multiplexing, Channel Modeling, Rank Codes, and their Applications, and Internet of Things (IoT).